

# Versatile tabletop setup for picosecond time-resolved resonant soft-x-ray scattering and spectroscopy

Cite as: Rev. Sci. Instrum. 94, 063102 (2023); doi: 10.1063/5.0151613

Submitted: 23 March 2023 • Accepted: 31 May 2023 •

Published Online: 26 June 2023



View Online



Export Citation



CrossMark

Martin Borchert,<sup>1</sup> Julia Braenzel,<sup>1</sup> Richard Gnewkow,<sup>2,3,4</sup> Leonid Lunin,<sup>1</sup> Themistoklis Sidiropoulos,<sup>1</sup> Johannes Tümmeler,<sup>1</sup> Ingo Will,<sup>1</sup> Tino Noll,<sup>1</sup> Oliver Reichel,<sup>1</sup> Dirk Rohloff,<sup>1</sup> Alexei Erko,<sup>5,a)</sup> Thomas Krist,<sup>6</sup> Clemens von Korff Schmising,<sup>1</sup> Bastian Pfau,<sup>1</sup> Stefan Eisebitt,<sup>1,3</sup> Holger Stiel,<sup>1,4,b)</sup> and Daniel Schick<sup>1,b)</sup>

## AFFILIATIONS

<sup>1</sup>Max-Born-Institut für Nichtlineare Optik und Kurzzeitspektroskopie, 12489 Berlin, Germany

<sup>2</sup>Helmholtz-Zentrum Berlin, 12489 Berlin, Germany

<sup>3</sup>Technische Universität Berlin, Institut für Optik und Atomare Physik, 10623 Berlin, Germany

<sup>4</sup>Berlin Laboratory for Innovative X-ray Technologies (BLIX), 10623 Berlin, Germany

<sup>5</sup>IAP eV, 12489 Berlin, Germany

<sup>6</sup>NOB Nano Optics Berlin GmbH, 10627 Berlin, Germany

<sup>a)</sup>A. Erko deceased during the creation of the presented studies on the 22nd of October 2022.

<sup>b)</sup>Authors to whom correspondence should be addressed: [stiel@mbi-berlin.de](mailto:stiel@mbi-berlin.de) and [schick@mbi-berlin.de](mailto:schick@mbi-berlin.de)

## ABSTRACT

We present a laser-driven, bright, and broadband (50 to 1500 eV) soft-x-ray plasma source with <10 ps pulse duration. This source is employed in two complementary, laboratory-scale beamlines for time-resolved, magnetic resonant scattering and spectroscopy, as well as near-edge x-ray absorption fine-structure (NEXAFS) spectroscopy. In both beamlines, dedicated reflection zone plates (RZPs) are used as single optical elements to capture, disperse, and focus the soft x rays, reaching resolving powers up to  $E/\Delta E > 1000$ , with hybrid RZPs at the NEXAFS beamline retaining a consistent  $E/\Delta E > 500$  throughout the full spectral range, allowing for time-efficient data acquisition. We demonstrate the versatility and performance of our setup by a selection of soft-x-ray spectroscopy and scattering experiments, which so far have not been possible on a laboratory scale. Excellent data quality, combined with experimental flexibility, renders our approach a true alternative to large-scale facilities, such as synchrotron-radiation sources and free-electron lasers.

© 2023 Author(s). All article content, except where otherwise noted, is licensed under a Creative Commons Attribution (CC BY) license (<http://creativecommons.org/licenses/by/4.0/>). <https://doi.org/10.1063/5.0151613>

## I. INTRODUCTION

The soft-x-ray range provides unique spectral fingerprints for a plethora of microscopic processes relevant to physics, material science, chemistry, and biology. By covering the absorption  $K$ -edges of the organic elements O, N, and C, as well as the  $L$ - and  $M$ -edges of most transition metals (TMs) and rare earths (REs), respectively, soft x rays are an indispensable tool for studying, e.g., photosynthesis,<sup>1</sup> catalysis,<sup>2–4</sup> materials for batteries,<sup>5</sup> solar cells,<sup>6,7</sup> or magnetism.<sup>8–10</sup> In addition to the spectral sensitivity, the short wavelengths of soft x rays enable scattering techniques to access spatial

information on the nanometer scale. Until recently, soft x rays have been exclusively available at large-scale facilities such as synchrotron-radiation facilities or free-electron lasers (FELs) for such experiments. The intrinsic pulse duration of these sources, ranging from hundreds of picoseconds down to few-femtoseconds, allowed for a variety of time-resolved studies of photo-induced dynamics using soft x rays.<sup>11,12</sup> Due to the limitations in access and flexibility of large-scale facilities and driven by the continuous development of high-power, ultrashort optical laser systems, new laboratory sources have been developed, covering the soft-x-ray spectral range. While higher harmonic generation (HHG) sources

are readily covering the photon energy range up to the *water window* at photon energies of  $E = 280\text{--}530$  eV,<sup>13–17</sup> time-resolved experiments above this range have not been possible in a laser laboratory, so far.

In this work, we describe a tabletop setup for picosecond soft-x-ray resonant scattering and spectroscopy experiments, well beyond the water window. For that, we employ the broadband emission of a laser-driven plasma x-ray source (PXS) from  $E = 50\text{--}1500$  eV. We developed and installed two complementary beamlines, both relying on custom reflection zone plate (RZP) optics for the soft-x-ray regime, which capture, disperse, and focus a large part of the generated broadband radiation. The first beamline is designed to study magnetic materials by means of magnetization-sensitive spectroscopy and resonant magnetic scattering techniques. Its endstation hosts the necessary goniometer, cryostat, and electromagnet for accessing reciprocal space and for full environmental control of the magnetic samples. The second beamline is specifically tailored for near-edge x-ray absorption fine structure (NEXAFS) spectroscopy, covering a spectral range of up to 300 eV in a single acquisition with a remarkable spectral resolution of  $E/\Delta E = 500\text{--}1000$  eV by using a hybrid RZP design on curved substrates.<sup>18</sup> Both beamlines allow for optical excitation of the samples via synchronized pump laser pulses.

## II. SETUP

First attempts to study laser-produced plasmas as potential soft-x-ray sources for applications in spectroscopy and imaging date back to the 1970s.<sup>19,20</sup> Later, their development received a major boost from the industry demanding new short-wavelength

and monochromatic light sources for lithography.<sup>21,22</sup> The application of a PXS for spectroscopy and resonant scattering in the soft-x-ray regime, however, requires a bright and quasi-continuous emission spectrum as achieved by solid-state target systems based on high-atomic number materials.<sup>23,24</sup> Here, we extend this principle beyond typical driver lasers with nano- or sub-nanosecond pulse duration<sup>25–27</sup> by employing picosecond pulses from a high-power thin-disk laser system onto metallic targets, such as tungsten. The generated plasma delivers a high photon flux in the soft-x-ray range from  $E = 50\text{--}1500$  eV and enables ultrafast pump-probe experiments with a temporal resolution of  $<10$  ps.<sup>28</sup> Comparable to large-scale facilities, the operation of the PXS and its beamlines requires a multitude of hard- and software components to work together in a safe and reliable way. In Secs. II A–II D, we describe the type of implementation and specifications of the most important components, which are also depicted in the schematic overview in Fig. 1.

### A. Laser system

The driving laser is an in-house-developed thin-disk laser system,<sup>29</sup> designed to deliver high pulse energies at a remarkable stability ( $>220$  mJ  $\pm$   $<0.2\%$  [rms]) at 100 Hz repetition rate and a wavelength of 1030 nm, cf. Fig. 1. Its frontend is based on an Yb:KGW oscillator, emitting laser pulses in the nJ energy range with 100 fs pulse duration. A pulse picker reduces the repetition rate from 80 MHz down to 100 Hz and the remaining pulses are stretched in time<sup>30</sup> by a grating stretcher prior to pre-amplification to about 1 mJ by a Yb:KGW regenerative amplifier. Afterward, the beam is enlarged and fed into the main regenerative amplifier stage, based on a 500  $\mu\text{m}$  thin Yb:YAG disk with a diameter of 14 mm, with the

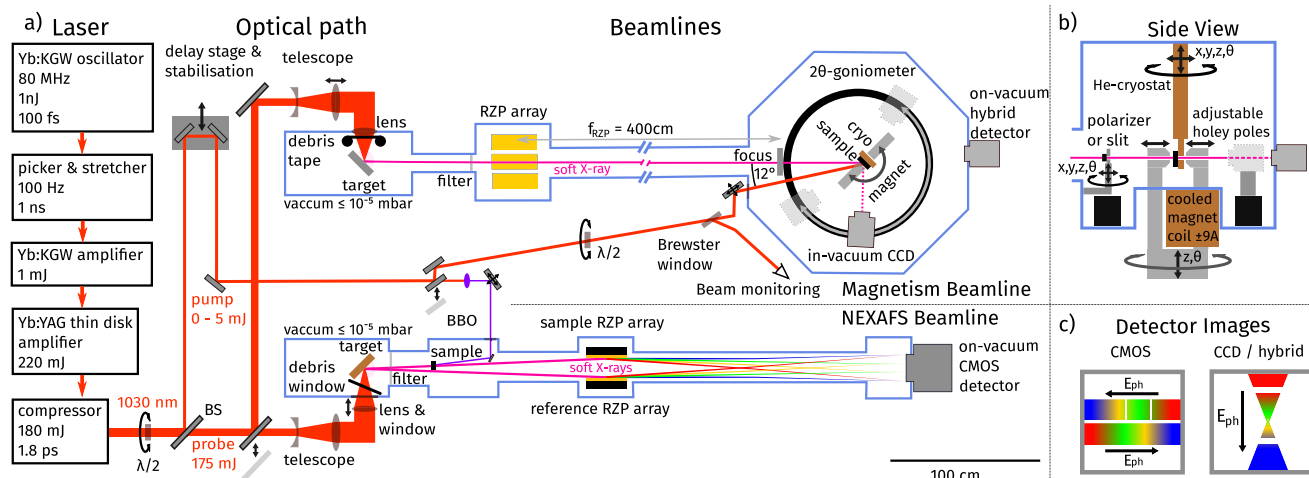


**FIG. 1.** Schematic overview of the laboratory setup with laser components, optical path, and beamlines for magnetism (top) and NEXAFS spectroscopy. (a) Amplified laser pulses are separated at a beamsplitter (BS) into a driving beam for the plasma generation and a delayable pump beam, both to be sent into either beamline. The driving beam is focused onto a metallic target (vacuum of  $<1 \times 10^{-5}$  mbar, blue outline), emitting soft x rays into the full solid angle, captured, focused, and dispersed by reflection zone plate (RZP) arrays. (b) Side view of the magnetism end station, featuring an optional magnetic thin film polarizer or variable slit, an on-vacuum electromagnet with its magnetic poles feeding into the vacuum, and a closed-cycle He-cryostat. A slow-readout in-vacuum charge-coupled device (CCD) camera on a  $2\text{-}\theta$  goniometer or a kHz-readout on-vacuum hybrid detector on the far end of the chamber is used to detect transmitted or scattered soft x rays. (c) Typical detector images for the NEXAFS (left) and magnetism (right) beamline. The plane of dispersion between both beamlines is rotated due to the different orientations of the RZP arrays.

center 10 mm pumped by two 1 J/ms diode banks via fiber couplers. The uncompressed pulses reach energies of up to >220 mJ with a bandwidth of 1 nm full width at half maximum (FWHM) and a duration of 1 ns FWHM. Finally, the beam is spatially cleaned by passing through a pinhole and its diameter is enlarged by a factor of five to about 25 mm FWHM before being temporally compressed by a grating compressor down to 1.8 ps FWHM with a transmission efficiency of  $\approx 80\%$  yielding a pulse energy of  $\approx 180$  mJ.

For optimizing the data acquisition in terms of speed and signal to noise, and for minimizing the debris generation of the PXS, it is essential to generate well-defined and synchronizable single pulses or pulse trains with the thin-disk laser; see Secs. II B and II C. For this, we combine a fast shutter (SH05R/M with SC10 controller, Thorlabs, Inc.), blocking the lower power seed beam before the thin-disk amplifier with slower motorized flip-mirror mounts, guiding the amplified laser after the thin-disk amplifier into a beam dump outside the laser when not used in the experiments. With this combination, we are able to minimize unseeded periods of the thin-disk laser, avoiding thermal non-equilibrium, while enabling also flexible pulse sequences to excite the PXS targets.

The compressed laser pulses are further split into a driving beam for the PXS (175 mJ pulse energy) and a pump beam for photo-exciting the samples (5 mJ pulse energy) via a rotatable half-wave plate and a subsequent polarization-dependent beamsplitter. The pump beam can be delayed by traversing up to 2 m of the additional optical path (6.6 ns) along a linear, motorized delay line, incorporating pointing-stabilization by stepper-piezo dual mirrors (Aligna 4D, TEM Messtechnik GmbH). Prior to entering the vacuum, the PXS driving beam is first enlarged by a 1:2 telescope to a diameter of  $\approx 50$  mm FWHM and eventually focused to a spot size of 15  $\mu\text{m}$  FWHM onto a metal target to create the plasma; see Sec. II B. Both the PXS driving laser and the probe laser beams can be directed into either beamline by mechanical flip mirrors.

## B. Soft-x-ray generation

At the focus of the optical laser, we reach peak intensities of over  $5 \times 10^{16}$  W/cm<sup>2</sup> that ionize the solid target material, igniting a plasma. In the excited plasma, line emissions and stochastic recombinations take place, which together with Bremsstrahlung result in an emission of incoherent, unpolarized soft-x-ray radiation covering a wide spectral range into the full solid angle.

Figure 2 shows the emission spectra from W and Cu targets obtained with a spectrometer setup, recently calibrated at the German National Metrology Institute (PTB Berlin).<sup>31</sup> For tungsten, with its high atomic order number, the emission lines are merged into a continuum spanning the spectral range from 50 to 1500 eV. We observe a photon flux of  $1 \times 10^8$  photons/s/mm<sup>2</sup>/mrad<sup>2</sup>/0.1% for high energies, increasing by more than two orders of magnitude to  $2 \times 10^{10}$  photons/s/mm<sup>2</sup>/mrad<sup>2</sup>/0.1% for lower photon energies. In contrast, the emission spectrum of copper is composed of discrete emission lines, however, with a significantly higher photon flux than the continuous spectrum of tungsten.

The metal targets are solid cylinders with a diameter of 50 mm and a length of 100 mm, made of pure metallic (>99.95%) tungsten, copper, or iron. Alternatively, foils of different materials can be attached to the cylinder.

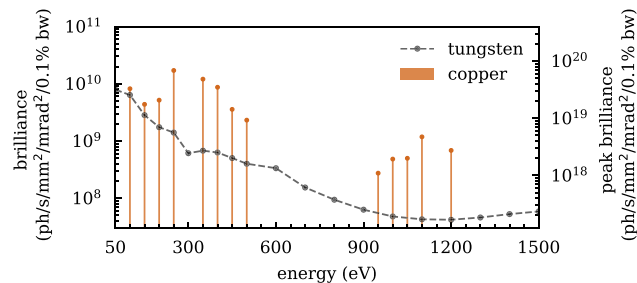


**FIG. 2.** Calibrated emission spectral measurements for Cu and W targets. Cu produces a line spectrum and W produces a quasi-continuous spectrum. Brilliance is calculated by assuming an average multi-shot spot diameter of 70  $\mu\text{m}$  (FWHM); see Fig. 3(b). The peak brilliance is calculated using the maximum pulse duration of 10 ps, the source repetition rate of 100 Hz, and a minimum single-shot spot diameter of 30  $\mu\text{m}$  (FWHM).

Due to the peak intensity of the laser, the top layer of the target is ablated for every single laser pulse, leaving a hemispherical crater with a diameter two to five times larger than the optical focus. To cope with the ablation craters on the surface of the target cylinders, we rotate them to avoid exposing the same spot on their surface with subsequent laser pulses. By additional translation of the cylinder along its rotation axis up to 2000 non-overlapping laser-cut grooves along the cylinder's circumference fit onto one target, assuming an average crater size of 50  $\mu\text{m}$  (FWHM). Without hitting the same spot twice, one target hence allows for more than 17 h of continuous measurement time. We typically prolong this time by one to two orders of magnitude by hitting target areas multiple times. However, such subsequent overlapping shots show a reduced photon flux, a change in the source position (pointing), and an increased source size of the soft-x-ray emission spot by defocusing. In addition, laser pointing fluctuations, mechanical instabilities, and imperfections of the target material affect the soft-x-ray emission spot.

The divergent soft-x-ray emission from the target is captured by Fresnel RZPs, which disperse the light along the plane of reflection, such as *standard* reflection gratings. However, in addition, these RZPs on planar substrates spatially focus the light in the perpendicular direction, with the tightest focus achieved for a specific design energy. Photons, whose energy matches this design energy, experience the highest spectral and spatial resolution, with all others focused less, yielding a distinct hourglass shape, as shown in the right part of Fig. 1(c). The focusing power of the RZPs is further dependent on the spot size and instabilities are translated into a decreased spectral resolution, as well as a pointing fluctuation of the soft-x-ray focus. Using curved instead of planar substrates yields a consistently high spectral resolution and focus size across a large spectral range, as shown in the left part of Fig. 1(c), as discussed in more detail in Sec. IV. The RZPs are mounted horizontally in the magnetism beamline and vertically in the NEXAFS beamline.

To quantify the instabilities in source size and pointing, we used a pinhole camera setup that images the source onto a detector with a magnification of 6.5 for different integration times, as shown in Figs. 3(a) and 3(b), respectively. By using a 500 nm aluminum filter and a 900 nm Mylar foil (see below), only photons with energies  $E > 300$  eV are transmitted toward the detector.

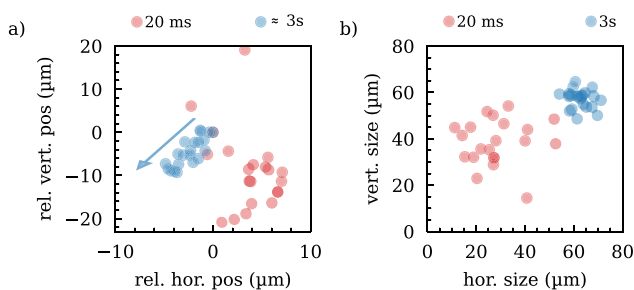


**FIG. 3.** Fluctuation of the soft-x-ray source in (a) spatial pointing and (b) source size (FWHM) for different integration times: 20 ms (2 shots, red) vs 2830 ms (283 shots, blue) per data point. The blue arrow in (a) indicates a drift of the target spot for repeated measurements.

As the laser is cutting a deeper groove into the target, the source spot position drifts over time, as indicated by the blue arrow in Fig. 3(a). For small integration times, e.g., 20 ms (2shots), a source size of  $(28 \pm 11) \mu\text{m} \times (38 \pm 9) \mu\text{m}$  FWHM is observed, as seen in Fig. 3(b). For longer integration times, e.g.,  $\approx 3$  s (283 shots), the fluctuations of pointing and de-focusing sum up to a bigger source size of  $(62 \pm 4) \mu\text{m} \times (57 \pm 3) \mu\text{m}$  FWHM, influencing the energy resolution of the subsequent RZP optics. These spectral drifts can be adjusted by minimizing the integration time (i.e., single or few shots) per acquisition and applying a drift correction of the individual spectra before averaging. In addition, the perpendicular translation stage allows us to move the target into the laser focus to correct for possible laser drifts.

As a by-product of the target ablation, the soft-x-ray emission is accompanied by debris of the target material, emitted in a wide cone, predominantly in the direction normal to the target, coating all surfaces in the surrounding. We implement different filter materials in order to prevent the optical components for the laser (entrance windows) and the soft-x-ray optics (RZPs) from being coated with the metallic debris. The entrance windows of the magnetism beamline are protected by a tape spooling device for optically transparent  $50 \mu\text{m}$ -thin films of polyester, allowing for multiple weeks of operation. To test an additional approach for handling the debris, we employ a  $100 \mu\text{m}$ -thin large aperture glass plate at the NEXAFS beamline, which is cleaned by the high intensity of subsequent laser pulses. In order to protect the RZP optics from debris, large-aperture ( $75 \times 75 \text{ mm}^2$ ) freestanding foils of mylar (thickness 900 nm) are placed between the PXS and RZP. Alternatively, free-standing ( $50 \times 50 \text{ mm}^2$ ) in-house-grown filters of, e.g., Al, Zr, or 3d (Fe, Co, Ni) and 5f (Gd, Dy, Tb) metals with thicknesses of 100–2000 nm can be used, which block most of the residual laser fundamental and also act as defined spectral filters in the soft-x-ray range.

### C. Timing and synchronization

For both beamlines, we use area detectors to acquire broad white-light spectra or spatially extended scattering profiles. While CCDs are typically slow in read-out, they feature low electronic noise. In contrast, complementary metal-oxide-semiconductor (CMOS) and hybrid-pixel<sup>32</sup> detectors enable fast read-out up to true-kHz frame rates enabling shot-to-shot acquisition at the full

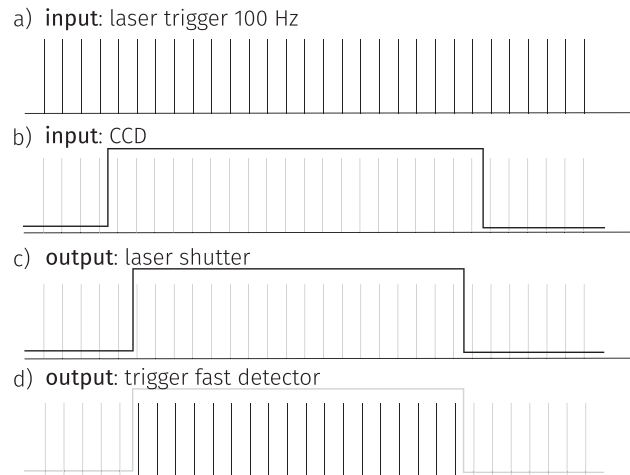


**FIG. 4.** Typical timing and synchronization scheme for both beamlines. (a) The 100 Hz laser trigger and (b) the CCD state are inputs of the PiLC. (c) The PiLC outputs a well-defined TTL gate for seeding the thin-disk laser. (d) Additionally, a defined number of 100 Hz trigger pulses only within the laser shutter gate can be output for fast detectors.

100 Hz repetition rate of the PXS. Here, it is essential to synchronize the PXS and the detectors such that a defined number of soft-x-ray pulses can be acquired. In addition, the soft-x-ray source must be blocked during read-out of the detectors, which is accomplished by a fast mechanical shutter in the driving laser; see Sec. II A. In order to realize the complex triggering and timing scheme, we employ a programmable-logic controller, based on a field-programmable gate array (FPGA), combined with a single-board computer (PiLC).<sup>33</sup> The PiLC features up to 16 input/output (IO) cards that we configured as digital IO with TTL level and interconnected them with typical logical operations via programming of the FPGA. The trigger scheme, as depicted in Fig. 4, shows the timing of laser trigger input, CCD input, and outputs to the laser shutter and fast detectors, such as CMOS, and hybrid-pixel detectors or digitizers for point detectors (photodiodes). For the CCD camera, we noticed a very large jitter when externally triggered, rendering single-pulse picking at 100 Hz impossible. We, therefore, use the CCD output indicating its integration period (TTL gate) as an input for the PiLC to enable the PXS during that period. The actual integration time of the CCD is typically extended by 20 ms to allow for delays of the mechanical shutter. During acquisitions without the CCD, the mechanical shutter is directly controlled by the PiLC to open for the next upcoming laser pulse. Detectors working at the full 100 Hz repetition rate receive the laser trigger signal that is gated by the opening window of the laser shutter.

### D. Control system and data acquisition

The operation of the setup presented is a complex task, as it requires the interplay of more than 50 devices, which are part of the laser, PXS, beamline, timing and synchronization, sample environment, as well as detection equipment. In order to ease the control,

configuration, and monitoring of this hardware, as well as the implementation of several software devices, we chose the free and open-source control system TANGO.<sup>34</sup> Within the TANGO framework, we benefit from experience and support by a community from large-scale facilities as well as from other comparable laboratory-scale experiments. In addition to the actual TANGO software bus, this includes specific software components, e.g., for building graphical user interfaces (synoptics), archiving and alarm systems, as well as ready-to-use drivers for many common hardware components—all provided with bindings to popular programming languages, such as C++, Java, Python, MATLAB, or LabView. In addition, TANGO has very low computing requirements and can be easily installed and run on popular single-board computers on different operating systems, such as Linux.

Based on the implementation of all hardware communication using the TANGO framework, we implemented the free and open-source Sardana software suite<sup>35</sup> for the actual data acquisition. Sardana handles the synchronized motion and acquisition of multiple motors and detectors, respectively. It further offers a flexible graphical user and command-line interface to define complex types of scans, such as scanning multiple motors, mesh scans, continuous/fly scans,<sup>36</sup> or reciprocal space scans. Sardana provides standardized data file handling, such as SPEC<sup>37</sup> and NeXus<sup>38</sup> file formats, and offers a macro-engine, which allows for user-defined measurement routines as well as for easy extension of its core functionalities. We use the later capability extensively to automatically switch between different operation modes of the laser and PXS, as well as to change the time and synchronization settings of the detection hardware depending on the current experiment at one of the two beamlines. With the level of automation, we minimize sources of error and make it easy for new users to carry out sophisticated measurements.

### III. MAGNETISM BEAMLINE

With its broadband emission in the soft-x-ray range, the PXS is perfectly suited for magnetism research, covering the relevant TM  $L_{2,3} - (2p \rightarrow 3d)$  and the RE element  $M_{4,5} - (3d \rightarrow 4f)$  absorption edges. For this, we set up a dedicated beamline [cf. Fig. 1(a) top] to carry out time-resolved resonant magnetic x-ray scattering (RMXS), as well as white-light x-ray magnetic circular dichroism (XMCD) spectroscopy at the TM  $L$ -edges in a laboratory environment, as discussed in Secs. III A and III B, respectively.

This beamline features an array of RZPs, each capable of capturing, dispersing, and focusing a specific bandwidth of the PXS spectrum to a focal plane inside the beamline's endstation. Here, three RZPs are mounted side-by-side on a five-axis in-vacuum manipulator with rapid alignment and switching capabilities. All RZPs are manufactured on planar substrates by electron-beam lithography, covered by a gold coating<sup>39,40</sup> with an angle of incidence of  $\alpha = 2^\circ$  and an angle of reflection for the first order of  $\beta = 3.6^\circ$ . The distance of the RZP array to the source of 1000 mm is a compromise between collecting a large solid angle of the PXS emission vs optimizing the focusing and resolving powers of the RZPs. We chose the focusing distance of all RZPs as  $f_{RZP} = 4000$  mm resulting in a nominal magnification of the PXS source spot by a factor of four in the focal plane to about 200  $\mu\text{m}$  FWHM with  $E/\Delta E > 500$ . Here, the resolution is limited by the size of the soft-x-ray spot on the target and

its fluctuations. A trade-off between target usage and measurement speed on one hand and high energy resolution and stability, on the other hand, has to be made (cf. Fig. 3). When investigating materials with featureless absorption peaks, like the  $L_3$  peak in pure Fe, for spectroscopy or scattering experiments, a lower resolution is acceptable. Reading out the detectors as fast as possible and shifting the resulting spectra, as demonstrated in our previous publication,<sup>41</sup> can mitigate the additional decrease in spectral resolution from pointing fluctuations. With typical absorption peaks featuring a spectral width of  $>1$  eV and typical optical excitation spot sizes in the order of  $\text{mm}^2$ , the spectral resolution and the focus size are well suited for time-resolved scattering experiments, which also benefit from the very low divergence of the soft-x-ray beam of only 0.5 mrad due to the large focal length  $f_{RZP}$ .

The RZPs are aligned such that their exit beam lies within the horizontal plane, which is equivalent to the scattering plane of the endstation while the RZP's dispersion direction is vertical. The typical hourglass-like x-ray distribution in the focus plane of the RZPs is sketched in the right part of Fig. 1(c), revealing the smallest spatial and spectral focus only for the specific design energy of each RZP. However, by slight detuning of the RZP's pitch angle,<sup>42</sup> using a piezo-driven goniometer (SGO-60.5, SmarAct GmbH), it is possible to vertically shift the x-ray pattern with an accuracy of  $<100$  meV, as well as to move the spectral focus slightly off its design energy. The relevant parameters of all RZPs available for the magnetism beamline are listed in Table I. Here, we also provide an estimate for the detectable photon flux at the sample position, taking the source flux, solid angle covered by the RZP, as well as the RZP's efficiencies into account.

The beamline's endstation features a flexible design to enable different magnetic scattering and spectroscopy techniques. The center of the vacuum chamber ( $\approx 900$  mm diameter) is placed 120 mm behind the RZPs' focus. Exactly at the focus, a variable horizontal slit is mounted to achieve the optimal monochromatization of the soft-x-ray spectrum. We added large SiC photodiodes (SG01XL, sglux GmbH) with an area of 7.6  $\text{mm}^2$  to each slit blade as close as possible to its gap. Both diodes are used for the normalization of the incoming soft-x-ray flux by detecting the blocked part of the spectrum at the slit. The SiC diodes are intrinsically insensitive to any residual optical laser light in the endstation because of their 3 eV band gap.

We realized a two-circle diffractometer with its rotation axis normal to the horizontal scattering plane in the center of the endstation. For the inner circle, a stepper-motor-actuated closed-cycle cryostat (CCS-XG-UHV/204N, Cryophysics GmbH) with vibration

**TABLE I.** Nominal RZP parameters and expected flux at the RZP focus with no filter or mylar foil in the beam.

Element	Energy (eV)	Active area $\text{mm}^2$	Efficiency (%)	flux (ph/s)/eV
Fe	715	$80 \times 12$	18	$4.3 \times 10^6$
Co	785	$82 \times 12$	18	$2.4 \times 10^6$
Gd	1200	$80 \times 7$	8.3	$1.6 \times 10^5$
Dy	1300	$80 \times 7$	6.3	$1.2 \times 10^5$

damping and a temperature range from 30 to 500 K is mounted to the top of the chamber, allowing for sample rotation ( $\vartheta$ ) in the scattering plane, as well as linear motion in all three dimensions. An in-vacuum high-load rotational table (430 X2 W1 HV, HUBER Diffractionstechnik GmbH & Co. KG) forms the outer circle of the diffractometer ( $2\vartheta$ ) and rotates a height-adjustable breadboard for the soft-x-ray detectors and a photo diode in the horizontal scattering plane. The large aperture of the  $2\vartheta$ -goniometer further allows us to feed the poles of an on-vacuum electromagnet through the bottom of the chamber for magnetic manipulation of the sample. The coils of the electromagnet are kept in air and are water-cooled to reach magnetic fields of up to 1 T continuously and 1.5 T in the burst mode by simultaneously avoiding large heat generation in the vicinity of the samples. The magnet is height-adjustable and its field can be freely rotated within the scattering plane of the diffractometer with a variable gap between its poles.

The soft-x-ray detector on the  $2\vartheta$ -arm is a compact, water-cooled in-vacuum CCD camera (MTE-2 2048B, Teledyne Princeton Instruments) with  $2048 \times 2048$  pixels<sup>2</sup> of  $13.5 \times 13.5 \mu\text{m}^2$ . Any residual optical light is blocked by a self-grown (or commercial) large-area Al-filter  $50 \times 50 \text{ mm}^2$  ( $30 \times 30 \text{ mm}^2$ ) with thicknesses of 100–500 nm mounted in front of the CCD. Other point detectors such as photodiodes for the soft-x-ray or optical range can be variably mounted next to the CCD. Alternatively, an on-vacuum, hybrid silicon pixel detector (MOENCH, Paul Scherrer Institute)<sup>32</sup> is mounted  $\approx 600$  mm away from the sample in transmission geometry. Its short read-out time of 250  $\mu\text{s}$ , permitting a 100 Hz frame rate to record and read out every pulse, enables single-photon counting capabilities in the soft-x-ray regime.

For photoexcitation of the sample, we utilize up to 5 mJ of pulse energy, out-coupled from the driving laser. After delaying it via a mechanical delay stage by up to 6.6 ns, it is guided along the soft-x-ray beamline to an optical table next to the endstation. Here, the diameter of the pump beam is reduced, its slightly elliptical shape is rounded by a telescope, and its pulse energy is set by a combination of a  $\lambda/2$  wave plate and a Brewster window. We are constantly monitoring the power and position of the optical beam by guiding 4% of the beam's power onto a camera via a beam sampler. The pointing of the pump beam can be adjusted by a motorized mirror for optimizing the spatial overlap with the soft-x-ray probe-beam at the sample position.

### A. Resonant magnetic soft-x-ray scattering

Time-resolved resonant magnetic soft-x-ray scattering (RMXS) is a powerful tool for accessing element-specific spin dynamics in magnetic materials.<sup>43</sup> In particular, it allows us to probe the magnetic order parameter of antiferromagnetic (AFM) materials, which can hardly be studied by other techniques due to the absence of a net magnetic moment ( $\vec{M} = 0$ ). RMXS requires tunability of the probing soft-x-ray photon energy to match an elemental resonance, which is magnetically sensitive due to the x-ray magnetic circular dichroism effect (XMCD), cf. Sec. III B. At the same time, half of the wavelength  $\lambda$  must be smaller than the AFM periodicity to resolve it in reciprocal space. The resulting integral under the AFM Bragg peak and its peak position in reciprocal space are a

direct measure of the AFM order parameter and the periodicity, respectively.

To demonstrate the capability of the magnetism beamline for RMXS experiments, we study the magnetic and structural dynamics of an AFM-coupled Fe/Cr superlattice (SL).<sup>28</sup> The SL sample was grown by molecular beam epitaxy (MBE) on a GaAs substrate with a 150 nm thick Ag buffer, and 20 repetitions of 0.9 nm thick Fe and 0.9 nm thick Cr layers were added on top, with a 2 nm thick MgO layer as oxidation protection. Due to the interlayer-coupling through the Cr layers,<sup>44,45</sup> the individual Fe layers couple antiferromagnetically along the out-of-plane direction but stay ferromagnetically aligned in-plane. Both the structural and the AFM periodicities can, hence, be resolved at the Fe  $L_3$ -edge around 707 eV ( $\lambda = 1.8$  nm).

For tuning the soft-x-ray energy to this magnetically sensitive absorption edge, we first scan the RZP pitch angle at fixed slit width and position to reflect different parts of the PXS spectrum from the Fe/Cr SL at a small grazing incidence angle of  $\vartheta = 10^\circ$  ( $2\vartheta = 20^\circ$ ). The resulting reflection spectrum is depicted in Fig. 5(a) and reveals two maxima, which we assign to the Fe  $L_{2,3}$ -absorption edges. We can reproduce the spectrum using a polarization-dependent scattering formalism<sup>46</sup> simulation,<sup>47</sup> which is based on high-resolution atomic and magnetic form factors of the involved elements and a model of the sample's geometry. From fitting the simulations to the experimental data, we determine a spectral resolution of  $(1.5 \pm 0.2)$  eV, which is slightly larger than the expected resolution of 1.2 eV with a 100  $\mu\text{m}$  gap of the slit. We then fix the soft-x-ray photon energy to 680 eV (off-resonant) or 707 eV (resonant) to carry out  $\vartheta - 2\vartheta$ -scans ( $L$ -scans); see Fig. 5(b). The Bragg peak at  $L = 1.0$  rlu (reciprocal lattice units) is observable for both photon energies and is linked to the 1.8 nm structural periodicity of the Fe/Cr SL. The AFM Bragg peak at  $L = 0.5$  rlu is, however, only observable on resonance and is a direct measure of the AFM order, as discussed above. The scans, shown in Fig. 5, are the first resonant magnetic scattering results at the Fe  $L$ -edges acquired at a laser-driven soft-x-ray source; see our previous publication for more details.<sup>28</sup> We further evaluate the capabilities for time-resolved experiments at the magnetism beamline. For this purpose, we probe the evolution of the magnetic ( $L = 0.5$ ) Bragg peak after photoexcitation with an incident laser fluence of 66 mJ/cm<sup>2</sup>. The fast and steep drop of the AFM Bragg peak intensity, as shown in Fig. 6, is a clear indication of a laser-induced demagnetization of the ferromagnetic Fe layers in the SL sample. The transient data also allow us to determine the temporal resolution of the experiment to  $< 10$  ps by fitting it with an exponential decay function, convoluted by a Gaussian function of the width of the PXS's pulse duration.

To probe the structural dynamics of the lattice as a response to the same photoexcitation as before, we measure the reflected intensity slightly to the left of the maximum at  $L = 0.95$ . With this, the signal is very sensitive to peak shifts in reciprocal space. The increase in the diffracted intensity is a clear indication of a peak shift to lower  $L$ -values, which corresponds to a thermal expansion of the Fe/Cr SL in real space. The delay scan reveals a slower rise and a long-lived plateau, compared to the faster (sub-nanosecond) recovery of the AFM signal. With these results, we could show that the magnetism beamline allows us to probe AFM and lattice dynamics in one and the same experiment with high temporal and reciprocal-space resolution.

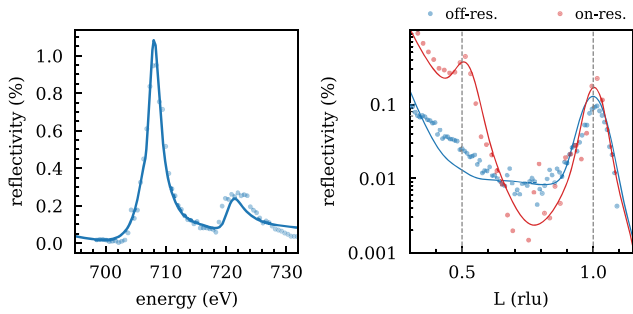


**FIG. 5.** Static RMXS results for a Fe/Cr superlattice under reflection with monochromatized light. Left: Reflection spectrum under a grazing incidence angle of  $\vartheta = 10^\circ$ ; measured by scanning the photon energy around the Fe  $L$ -edges across the sample. Right:  $\vartheta - 2\vartheta$ -scan/ $L$ -scan across the first magnetic ( $L = 0.5$ ) and structural ( $L = 1.0$ ) Bragg peaks with the photon energy tuned resonantly to the  $L_3$ -edge or off-resonantly away from it.

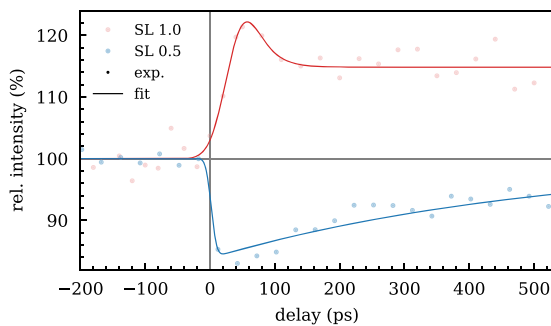


**FIG. 6.** Transient RMXS results for a Fe/Cr superlattice on the maximum ( $L = 0.5$ ) of the magnetic peak (blue, demagnetization) and slightly to the left ( $L = 0.95$ ) of the structural peak (cf. Fig. 5, right, on-res.) after laser excitation with a 1.8 ps pump pulse.

### B. X-ray magnetic circular dichroism spectroscopy

X-ray magnetic circular dichroism (XMCD)<sup>48–50</sup> describes the strong dichroic absorption of circularly polarized light when tuned near spin-split core-to-valence-band transitions in the extreme ultraviolet (XUV) to hard x rays.

Covering the TM  $L$ - and RE  $M$ -absorption edges, where the XMCD effect shows a very large magnetic contrast,<sup>51</sup> enables the separation of the orbital from the spin contributions to the local magnetic moments via the summation rules.<sup>52–54</sup>

While our setup easily meets the requirements for reaching the photon energies relevant for XMCD in the soft-x-ray regime, the emission from the PXS is intrinsically randomly polarized due to the incoherent emission processes in the plasma. However, by inserting a magnetic thin-film polarizer,<sup>55,56</sup> it is possible to achieve partial circular polarization of the PXS spectrum. We utilize this polarized light for the first XMCD experiments at the Fe  $L$ -edges at a laser-driven soft-x-ray source.<sup>41</sup>

This was achieved with a 100 nm thick polariser and a 55 nm thick sample, both made of a ferrimagnetic  $\text{Gd}_{0.24}\text{Fe}_{0.76}$  alloy with perpendicular anisotropy, sputtered on a 50 nm thick SiN membrane. Both films are capped and seeded by 3 nm of Ta and have a

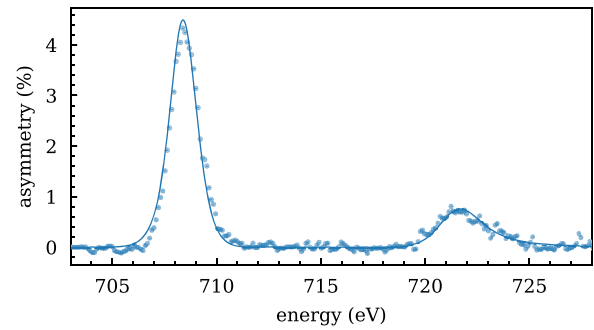


**FIG. 7.** Static XMCD results for a FeGd alloy sample in transmission geometry. Asymmetry, calculated from two dichroic white light transmission spectra. A signal-to-noise ratio (SNR) > 200 can be obtained within 340 s of integration time.

clear aperture of  $4 \times 4 \text{ mm}^2$ . The large aperture allows us to transmit the full spatially dispersed spectrum of the soft x rays in a white-light scheme through the polarizer, sample, and onto the CCD detector.

We aim the polarizer magnetization to point along the soft-x-ray propagation direction and vary the magnetization of the sample to be parallel and anti-parallel to it by a magnetic field of  $\pm 100 \text{ mT}$  provided by the electromagnet of the endstation. From both dichroic spectra, one can calculate the XMCD asymmetry as  $A = \frac{T^- - T^+}{T^- + T^+}$ ; see Fig. 7. The presented dataset was acquired within 170 s per magnetization direction with an SNR > 200 across the whole spectral range; see our previous publication for more details.<sup>41</sup> We can model the experimental transmission spectra, as well as the resulting asymmetry with high accuracy by magnetic scattering simulations,<sup>46,47</sup> which sensitively depend on the sample and polarizer geometries, as well as their experimentally determined atomic and magnetic scattering factors.<sup>57,58</sup> The presented results confirm the capabilities of the magnetism beamline for time-resolved XMCD spectroscopy with few-ps temporal and with a high  $E/\Delta E \approx 550$  spectral resolution.

### IV. NEXAFS BEAMLINE

This beamline is designed for high-resolution near-edge x-ray absorption fine-structure (NEXAFS) experiments in transmission geometry. As for the magnetism beamline, we usually choose tungsten as a target material, as it covers a wide photon energy range from 50 to 1500 eV with a quasi-continuum spectrum<sup>59</sup> in a single shot (cf. Fig. 2). In order to achieve the required high spectral resolution for NEXAFS spectroscopy, we designed a special two-channel detection system with two —ideally— identical RZPs as diffractive optics, a measurement channel and a reference channel. In contrast to earlier approaches, based on RZPs on planar substrates,<sup>60</sup> here, we present a prototype setup of an R&D project in cooperation with NOB Nano Optics Berlin GmbH, which uses novel hybrid RZP structures consisting of suitably designed RZPs on spherically curved substrates.

Commonly used RZPs on planar substrates (cf. Sec. III) only focus particular photon energies across a few-eV bandwidth spatially and spectrally onto a detector for a given RZP structure and RZP-to-detector distance. There, in order to cover the large energy range

of the source, multiple RZP structures are needed. Alternatively, slightly misaligning the planar RZP structures can shift the spectral position of optimal resolution. As a consequence, a large spectral range, covering more than 200 eV, requires a time-demanding scan of different alignment positions, which needs to be stitched together.<sup>42</sup> In addition, in the RZP focal region of a given design energy, spatial imaging over a wide spectral range is not retained, which excludes spectral-spatial imaging. In order to overcome this, a novel approach for high-resolution and wide-spectral imaging is to use hybrid RZPs on spherical substrates, with optimized aberration-corrected zone plate structures.<sup>18</sup> These hybrid RZPs provide high resolution  $E/\Delta E > 500$  over a wide spectral range of  $E = 130\text{--}550$  eV and reaching up to  $E/\Delta E < 1000$  over smaller energy ranges. The efficiency is comparable to planar RZP optics, while retaining one spatial dimension for imaging.

Both the measurement and reference prototype RZPs each combine four different zones on one single curved substrate with a radius of curvature  $R = 43\,922$  mm, covering a spectral range from  $E = 210\text{--}1400$  eV. These four structures ( $S_i$ ) cover the following photon energy ranges:  $E = 210\text{--}345$  eV ( $S_1$ ),  $E = 340\text{--}550$  eV ( $S_2$ ),  $E = 550\text{--}880$  eV ( $S_3$ ), and  $E = 850\text{--}1404$  eV ( $S_4$ ). With an angle of incidence of  $\alpha = 2^\circ$  and an angle of reflection for the first order of  $\beta = 3.65^\circ$ , the RZPs are offset laterally by 66.25 mm on either side of the optical axis that connects the target and the detector. Each structure has an active area of  $3.7 \times 80$  mm<sup>2</sup>. The capturing aperture for the prototype is only limited by the number of structures that needed to be placed on the substrate. The RZPs have been characterized at the German National Metrology Institute (PTB Berlin), regarding their efficiency and did reach the theoretically expected values. For full, fine motion control, both RZPs are mounted on their own six-axis hexapod (SMARPOD 110.45.1-D-S-HV, Smaract GmbH), allowing a precise alignment of the soft-x-ray beam onto the detector. By small deviations from the nominal angles of the RZP, the spectral range can be extended down to 100 or up to 1500 eV, with a sufficiently high  $E/\Delta E$ .

For a fast data acquisition, the setup is equipped with one of two 16-bit scientific complementary metal-oxide-semiconductor (sCMOS) detectors ( $2048 \times 2048$  pixels<sup>2</sup>,  $11 \times 11$   $\mu\text{m}^2$  (modified Dhyana90 400D TUCSEN, Tucsen Photonics Co. Ltd. or AXIS-SXRF-V2-EUV, AXIS Photonics, Inc., Canada). The detector is placed at a distance of  $f_{\text{RZP}} = 2040$  mm from the RZPs. If the full chip is read out, we reach maximum frame rates of 24 Hz at 16-bit or 48 Hz at 12-bit resolution, respectively. With a smaller region of interest ( $480 \times 2048$  pixels<sup>2</sup>), we can match the data acquisition to the laser repetition rate of 100 Hz at a 16-bit resolution, enabling single laser shot measurements.

The hybrid RZPs, together with the  $<300$  ms-read-out of the detector, significantly decrease the measurement time for comparable laboratory-based NEXAFS beamlines using a conventional CCD detector and planar RZPs.<sup>42</sup> The spectral range for each measurement spans the full bandwidth, e.g., for the  $S_4$  structure ( $E = 850\text{--}1400$  eV). In view of long measurement sequences that are required for future time-resolved measurements and needed transient NEXAFS signal down to  $1 \times 10^{-3}$ , the significantly faster measurement acquisition of 10 Hz (in comparison to the readout delay of conventional CCD detectors, only considering one spectral position) is a big step forward for laboratory-based soft-x-ray NEXAFS beamlines.

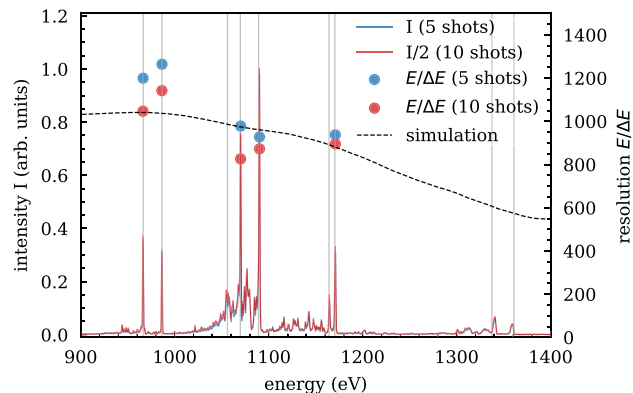


**FIG. 8.** Averaged spectra of copper atomic line emission spectrum from 14 measurements of 5 or 10 laser pulses each using the hybrid RZP  $S_4$  structure. The measurements are pointing corrected in the post-processing, and gray lines indicate identified theoretical positions of the atomic lines of CuXX. The black dashed line shows the theoretical resolution from a simulation for the used setup and optics using the RAY-UI software.<sup>61,62</sup> The line energies are taken from the American National Institute of Standards and Technology database.<sup>63,64</sup>

For characterizing the novel hybrid RZPs at this PXS, the W target was replaced by a Cu target, emitting an atomic line spectrum with strong, well-known emission lines in the range of  $E = 900\text{--}1400$  eV, as shown in Fig. 8. By limiting the integrated shot numbers for each measurement and correcting the obtained spectra for spectral pointing of the PXS, we reach, in the spectral range of  $E = 900\text{--}1200$  eV, the theoretical resolving power. As the resolution is a function of the source size, our peak resolution of  $\Delta E/E = 1200$  for the CuXX lines at 996 and 986 eV exceeded the simulated resolution<sup>61,62</sup> due to a slightly smaller source size. The peaks in the higher spectral range  $>1300$  eV are not considered for evaluation because of their too-low dynamic range and overlap with background signal and multiplet lines. A small decrease in the resolution with a longer integration time can be concluded and is explained by an increase in the source size with longer integration times due to jitter.

Samples for NEXAFS measurements in transmission geometry are placed  $\approx 330$  mm away from the target in the downstream line to the detection channel RZP. At the sample position, the viewing area of the RZP structure is  $1.7 \times 1.7$  mm<sup>2</sup>. The light transmitted through the sample is captured, dispersed, and focused by the measurement channel RZP onto the upper half of the sCMOS detector. These samples usually consist of a few hundred nanometer thick films of a material of interest, deposited, e.g., on a  $\text{Si}_3\text{N}_4$  membrane (typical thickness of 200 nm and a size of  $0.25\text{--}9$  mm<sup>2</sup>), placed on a three-axis sample holder.

### A. NEXAFS spectroscopy

In contrast to optical spectroscopy, x-ray-based methods can yield access to structural, electronic, and chemical information about investigated atomic and molecular systems as they provide element-selective access to the system on an atomic level.<sup>27,65</sup> Laboratory-based NEXAFS via the outlined efficient and broadband RZPs

as dispersive optics provide, rapid, direct access to the absorption  $K$ -edges of organic compounds,  $M$ - and  $L$ -edges of TMs, and the  $N$ - and  $M$ -edges of REs. Besides their importance as functional units in organic compounds, TM compounds are widely used as functional materials in catalysis and photovoltaics. Optically induced photo processes in these materials can be readily probed by  $L$ -edge NEXAFS spectroscopy.<sup>66,67</sup> Transition metal compounds such as NiO and TiN are possible candidates for use in hydrogen production from water<sup>68</sup> and as an anode material in lithium batteries.<sup>69</sup>

In Secs. IV A 1 and IV A 2, we will demonstrate the performance of our setup for NEXAFS spectroscopy on  $L$ -edges of NiO, Ti, and TiN on  $\text{Si}_3\text{N}_4$  and Si membranes. The optical density (OD) obtained in these experiments is defined as the logarithmic ratio of the intensity transmitted through the sample  $I_s(E)$  and the intensity transmitted through the reference  $I_r(E)$ , e.g., the above-mentioned  $\text{Si}_3\text{N}_4$  membrane,

$$\text{OD}(E) = -\ln\left(\frac{I_s(E)}{I_r(E)}\right). \quad (1)$$

We further evaluate the detection limits of the setup for envisaged transient NEXAFS investigations.

### 1. NiO on $\text{Si}_3\text{N}_4$

With an early prototype hybrid RZP, with comparable parameters as mentioned above (same angle, 1.5 m distance from source, and same distance to detector), we qualitatively investigated the spectral resolution as a consequence of the spatial source jitter that increases the source size when integrating over many pulses. In addition, the jitter causes a small spectral displacement of the spectrum on the detector (few px), which can be corrected in post-processing for measurement sequences with a limited number of integrated pulses.

Here, we present near-edge x-ray absorption fine structure (NEXAFS) spectroscopy<sup>70</sup> results at the  $L_{3,2}$ -edges of Ni. NiO's  $L_2$ -edge exhibits a peak splitting at  $E = 871$  eV that becomes discernible with a resolving power of  $E/\Delta E > 1000$ ,<sup>71</sup> making it a suitable test system to study the energy resolution. For this, a 300 nm thick NiO (48:51) alloy sample was prepared on a 200 nm thick  $\text{Si}_3\text{N}_4$  window with an aperture of  $3 \times 3$  mm<sup>2</sup> by depositing Ni using a reactive electron beam evaporation in an oxygen environment at room temperature. The thickness was monitored with a quartz crystal balance, and the stoichiometry via energy dispersive x-ray spectroscopy measurements. To show the impact of the source jitter on the spectral resolution, we measured the NiO spectra with different single measurement integration times: 2, 5, and 10 pulses each, always acquiring a total number of 100 pulses. For each measurement sequence, the single spectra were pointing-corrected in post-processing before averaging the sequence. Figure 9 shows the resulting NEXAFS absorption spectra that exhibit a degradation in the resolution of the spectral features with an increasing number of pulses per measurement, discernible at the peak of the  $L_2$ -edge at 871 eV.<sup>72</sup> In our measurements, we could not fully resolve the peak splitting, but the onset of this feature is apparent for two laser shot measurements. A higher amount of laser shots clearly lowers the spectral resolution. Therefore, to reach the theoretical design resolution of the hybrid-RZPs of  $500 < E/\Delta E < 1000$  and for a sufficient dynamic range of the signal,

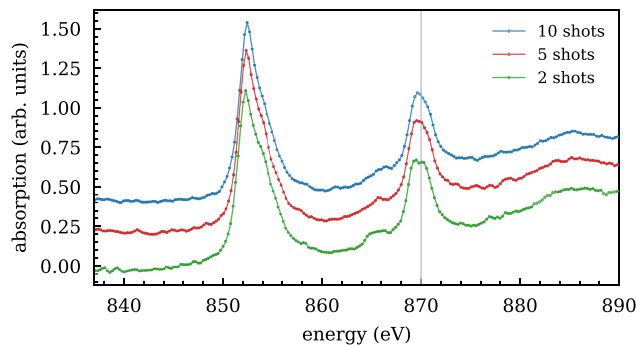


**FIG. 9.** NEXAFS spectra from 300 nm NiO on 200 nm  $\text{Si}_3\text{N}_4$  membrane demonstrating the spectral resolution as a function of a number of shots per measurement series. Longer integration times correspond to an averaged and, by the pointing, bigger source size, leading to a decrease in the spectral position. With sequences of close-to-single-shot acquisition, the spectral resolution can be increased, which is exemplified in the NiO  $L_2$  line splitting at 871 eV (gray line). The  $L_2$  splitting of Ni is yet not fully resolved, but becomes visible for pointing-corrected evaluation on image series with close-to-single-shot acquisition. Curves are offset for better visibility.

multiple single acquisitions with few shots each need to be taken, corrected, and averaged.

### 2. TiN and Ti on Si

The 100 nm thick TiN and Ti samples were grown on 50 nm thick  $500 \times 500$   $\mu\text{m}^2$  Si membranes by electron beam evaporation of Ti and in case of TiN under a  $\text{N}_2$ -rich atmosphere at a background pressure of  $6 \times 10^{-5}$  mbar. Both samples were measured using the  $\text{S}_2$  RZP structure of our prototype RZP and the sCMOS detector in a high dynamic range mode with a frame rate of 100 Hz. The NEXAFS spectra of Ti and TiN are shown in Fig. 10 across the Ti  $L$ -edge, as well as the  $K$ -edge of the organic element N. For Ti, we acquired 600 measurements at 100 Hz repetition rate with 10 pulses each, and for TiN, we acquired 2400 measurements with 5 pulses each. Both spectra are normalized to a measurement series without any samples, as in our prototype setup, and the second RZP channel was still in its commissioning phase. Our measurement of the near-edge absorption fine structure at the N  $K$ -edge of TiN is in excellent agreement with published data<sup>73,74</sup> (cf. inset of Fig. 10, numbers 1–6). For the spectra recorded, we have verified that the noise in the spectra presented is solely counting statistics-limited, without further contributions from detector noise or instabilities in the setup.

The key advantage of the setup is the ability to measure a NEXAFS spectrum in parallel over a large spectral range while still maintaining a resolving power up to  $E/\Delta E < 900$  and without compromising spectrometer efficiency. This dispersive acquisition mode covering an unprecedentedly large energy interval at full resolving power allows recording the NEXAFS region of one or even several atomic elements within a sample simultaneously. This results in a very substantial reduction of acquisition times. For example, the NiO spectra in Fig. 9 can be acquired in 0.1 s or less, including all overhead times for the measurement. To demonstrate that it is possible to reach outstandingly low fluctuation due

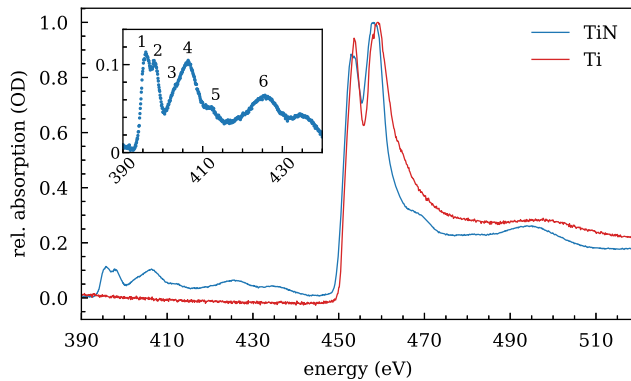


**FIG. 10.** TiN and Ti on Si membrane NEXAFS spectra. The inset shows a zoom into the N *K*-edge of TiN at  $E = 390\text{--}430$  eV to present the well-resolved characteristic spectral features of TiN, and numbers correspond to characteristic peaks from Pflüger *et al.*<sup>73</sup>

to counting statistics and, hence, the absence of significant (non-correctable) drifts or other instabilities, the TiN NEXAFS spectrum in Fig. 10 including the N *K*- and Ti *L*-absorption was integrated for 250 s. In view of future pump-probe NEXAFS experiments exploiting the 10 ps pulses of our source, the ability to measure spectra within minutes as well as the stability to do so over hours will be crucial to acquire full time traces following transient spectral changes.

## V. CONCLUSION AND OUTLOOK

In this work, we realized a versatile tabletop instrument for transient resonant scattering experiments, as well as NEXAFS and XMCD spectroscopy throughout the entire soft-x-ray regime. Our setup comprises a  $<10$  ps, broadband plasma x-ray source, driven by a high-power, high-stability thin-disk laser system. In combination with customized x-ray optics, advanced data acquisition schemes, and 2D detectors with frame rates exceeding the laser repetition rate of 100 Hz, we enable experimental methods in a laser laboratory, which have been limited to accelerator-based large-scale facilities so far. The broadband nature of the source enables us to perform white-light measurements across a wide range of photon energies in parallel, in contrast to energy scanning methods commonly used at these large-scale facilities.

At the magnetism beamline, an RZP-based monochromator allows for resonant scattering experiments at the TM *L*- and RE *M*-edges. We have demonstrated that it is possible to probe, e.g., the photo-induced dynamics of antiferromagnetic order at a time resolution of  $<10$  ps.<sup>28</sup> Furthermore, by using a wider range of photon energies and introducing a ferrimagnetic polarizer,<sup>41</sup> we also realized the first XMCD spectroscopy at the Fe *L*-absorption edges on a laboratory scale, achieving an SNR  $> 200$  within a matter of minutes via a white-light recording technique.

At the NEXAFS beamline, we employed hybrid RZPs where the curved substrates allow for a consistent spatial focus and high spectral resolution of  $500 < E/\Delta E < 1000$  across wide parts of the soft-x-ray spectrum. By correcting the spectral and pointing fluctuations of the soft-x-ray source by alternating measurement sequences

and additional post-processing procedures, we are able to record spectra with a noise floor that is purely counting statistics-limited. Due to the high efficiency of the RZPs and the use of an sCMOS camera, the data acquisition time was reduced by a factor of nearly 100 compared to previous work,<sup>60</sup> allowing to record transient NEXAFS spectra in periods of hours instead of days.

Our development enables the use of soft x-ray-based techniques in a laser laboratory, which has so far been exclusively the domain of work at large-scale facilities. Beyond enabling such experiments for a larger user base, e.g., at university departments or industrial applications, we note that performing such types of experiments at laser laboratories allows for the realization of sophisticated custom schemes for optical control of materials, which can be interrogated by powerful soft-x-ray approaches.

## ACKNOWLEDGMENTS

We like to acknowledge valuable discussions with Christian Schüßler-Langeheine, Niko Pontius, and Karsten Holldack about the magnetism beamline and diffractometer layout. We like to thank Tobias Spitzbart for helping with the PiLC setup. M.B., C.v.K.S., and S.E. would like to thank DFG for funding through Grant Nos. TRR227 and A02. J.B. and H.S. would like to thank EFRE for funding Grant No. ProFit project *MOSFER* 10168892. Part of this project has received funding from the European Union's Horizon 2020 research and innovation program under Grant Agreement No. 871124 Laserlab-Europe. D.S. would like to thank the Leibniz Association for funding through Grant No. Leibniz Junior Research Group J134/2022. We mourn the loss of our former colleague Professor Dr. Alexei Erko who passed away during the writing of this publication. Our thoughts go out to his family, his wife, his two children, and his grandchildren.

## AUTHOR DECLARATIONS

### Conflict of Interest

The authors have no conflicts to disclose.

### Author Contributions

**Martin Borchert:** Conceptualization (equal); Data curation (equal); Investigation (equal); Methodology (equal); Software (equal); Visualization (equal); Writing – original draft (equal); Writing – review & editing (equal). **Julia Braenzel:** Conceptualization (equal); Data curation (equal); Funding acquisition (supporting); Investigation (equal); Methodology (supporting); Software (supporting); Writing – original draft (equal); Writing – review & editing (equal). **Richard Gnewkow:** Conceptualization (supporting); Data curation (equal); Investigation (equal); Methodology (supporting); Software (supporting); Writing – original draft (equal); Writing – review & editing (equal). **Leonid Lunin:** Investigation (supporting); Methodology (supporting); Resources (supporting); Software (supporting); Writing – original draft (supporting); Writing – review & editing (equal). **Themistoklis Sidiropoulos:** Conceptualization (equal); Data curation (supporting); Funding acquisition (equal); Investigation (supporting); Methodology (equal); Resources (supporting);

Software (lead); Supervision (lead); Visualization (supporting); Writing – original draft (supporting); Writing – review & editing (supporting). **Johannes Tümmeler**: Conceptualization (supporting); Investigation (supporting); Methodology (supporting); Resources (equal); Writing – review & editing (equal). **Ingo Will**: Conceptualization (supporting); Investigation (supporting); Methodology (supporting); Resources (supporting); Writing – review & editing (supporting). **Tino Noll**: Conceptualization (supporting); Investigation (supporting); Methodology (supporting); Resources (supporting); Writing – review & editing (supporting). **Oliver Reichel**: Conceptualization (supporting); Methodology (supporting); Resources (supporting); Software (supporting); Writing – review & editing (supporting). **Dirk Rohloff**: Conceptualization (supporting); Funding acquisition (equal); Methodology (supporting); Resources (supporting); Software (supporting); Writing – review & editing (supporting). **Alexei Erko**: Conceptualization (supporting); Funding acquisition (equal); Resources (supporting); Software (supporting); Writing – review & editing (supporting). **Thomas Krist**: Conceptualization (supporting); Funding acquisition (equal); Investigation (supporting); Methodology (supporting); Resources (supporting); Writing – review & editing (supporting). **Clemens von Korff Schmising**: Conceptualization (supporting); Data curation (supporting); Funding acquisition (equal); Investigation (supporting); Methodology (supporting); Resources (supporting); Supervision (lead); Writing – review & editing (equal). **Bastian Pfau**: Conceptualization (equal); Data curation (supporting); Funding acquisition (equal); Investigation (supporting); Methodology (supporting); Resources (supporting); Supervision (lead); Writing – original draft (equal); Writing – review & editing (equal). **Stefan Eisebitt**: Conceptualization (equal); Data curation (supporting); Funding acquisition (lead); Investigation (supporting); Methodology (supporting); Resources (supporting); Software (lead); Supervision (lead); Visualization (supporting); Writing – original draft (equal); Writing – review & editing (lead). **Holger Stiel**: Conceptualization (equal); Data curation (equal); Funding acquisition (equal); Investigation (equal); Methodology (equal); Resources (equal); Supervision (equal); Writing – original draft (equal); Writing – review & editing (equal). **Daniel Schick**: Conceptualization (equal); Data curation (equal); Funding acquisition (equal); Investigation (equal); Methodology (equal); Resources (equal); Software (equal); Supervision (equal); Visualization (equal); Writing – original draft (equal); Writing – review & editing (equal).

## DATA AVAILABILITY

The data that support the findings of this study are openly available in “Versatile tabletop setup for picosecond time-resolved resonant soft x-ray scattering and spectroscopy” repository, at <https://zenodo.org/record/7757734>.

## REFERENCES

<sup>1</sup>M. Kubin, J. Kern, S. Gul, T. Kroll, R. Chatterjee, H. Löchel, F. D. Fuller, R. G. Sierra, W. Quevedo, C. Weniger, J. Rehanek, A. Firsov, H. Laksmono, C. Weninger, R. Alonso-Mori, D. L. Nordlund, B. Lassalle-Kaiser, J. M. Glowina, J. Krzywinski, S. Moeller, J. J. Turner, M. P. Minitti, G. L. Dakovski, S. Korodov, A. Kawde, J. S. Kanady, E. Y. Tsui, S. Suseno, Z. Han, E. Hill, T. Taguchi, A. S. Borovik, T. Agapie, J. Messinger, A. Erko, A. Föhlisch, U. Bergmann,

R. Mitzner, V. K. Yachandra, J. Yano, and P. Wernet, *Struct. Dyn.* **4**, 054307 (2017).  
<sup>2</sup>A. Nilsson, J. LaRue, H. Öberg, H. Ogasawara, M. Dell’Angela, M. Beye, H. Öström, J. Gladh, J. K. Nørskov, W. Wurth, F. Abild-Pedersen, and L. G. M. Pettersson, *Chem. Phys. Lett.* **675**, 145 (2017).  
<sup>3</sup>D. Bazin and L. Guzzi, *Appl. Catal., A* **213**, 147 (2001).  
<sup>4</sup>J.-D. Grunwaldt and C. G. Schroer, *Chem. Soc. Rev.* **39**, 4741 (2010).  
<sup>5</sup>X. Zhou, S. Qiao, N. Yue, W. Zhang, and W. Zheng, *Mater. Res. Lett.* **11**, 239 (2023).  
<sup>6</sup>K. Khalili, L. Inhester, C. Arnold, R. Welsch, J. W. Andreasen, and R. Santra, *Struct. Dyn.* **6**, 044102 (2019).  
<sup>7</sup>H. Jun, H. R. Lee, D. Tondelier, B. Geffroy, P. Schulz, J.-É. Bourée, Y. Bonnassieux, and S. Swaraj, *Sci. Rep.* **12**, 4520 (2022).  
<sup>8</sup>I. Radu, K. Vahaplar, C. Stamm, T. Kachel, N. Pontius, H. A. Dürr, T. A. Ostler, J. Barker, R. F. L. Evans, R. W. Chantrell, A. Tsukamoto, A. Itoh, A. Kirilyuk, T. Rasing, and A. V. Kimel, *Nature* **472**, 205 (2011).  
<sup>9</sup>B. Pfau, S. Schaffert, L. Müller, C. Gutt, A. Al-Shemmary, F. Büttner, R. Delaunay, S. Düsterer, S. Flewett, R. Frömter, J. Geilhufe, E. Guehrs, C. M. Günther, R. Hawaldar, M. Hille, N. Jaouen, A. Kobs, K. Li, J. Mohanty, H. Redlin, W. F. Schlotter, D. Sticker, R. Treusch, B. Vodungbo, M. Kläui, H. P. Oepen, J. Lüning, G. Grübel, and S. Eisebitt, *Nat. Commun.* **3**, 1100 (2012).  
<sup>10</sup>C. E. Graves, A. H. Reid, T. Wang, B. Wu, S. de Jong, K. Vahaplar, I. Radu, D. P. Bernstein, M. Messerschmidt, L. Müller, R. Coffee, M. Bionta, S. W. Epp, R. Hartmann, N. Kimmel, G. Hauser, A. Hartmann, P. Holl, H. Gorke, J. H. Mentink, A. Tsukamoto, A. Fognini, J. J. Turner, W. F. Schlotter, D. Rolles, H. Soltau, L. Strüder, Y. Acremann, A. V. Kimel, A. Kirilyuk, T. Rasing, J. Stöhr, A. O. Scherz, and H. A. Dürr, *Nat. Mater.* **12**, 293 (2013).  
<sup>11</sup>C. Pellegrini, *Eur. Phys. J. H* **37**, 659 (2012).  
<sup>12</sup>C. Pellegrini, *Nat. Rev. Phys.* **2**, 330 (2020).  
<sup>13</sup>C. Spielmann, N. H. Burnett, S. Sartania, R. Koppitsch, M. Schnürer, C. Kan, M. Lenzner, P. Wobrowschek, and F. Krausz, *Science* **278**, 661 (1997).  
<sup>14</sup>E. A. Gibson, A. Paul, N. Wagner, R. Tobey, D. Gaudiosi, S. Backus, I. P. Christov, A. Aquila, E. M. Gullikson, D. T. Attwood, M. M. Murnane, and H. C. Kapteyn, *Science* **302**, 95 (2003).  
<sup>15</sup>S. M. Teichmann, F. Silva, S. L. Cousin, M. Hemmer, and J. Biegert, *Nat. Commun.* **7**, 11493 (2016).  
<sup>16</sup>C. Kleime, M. Ekimova, G. Goldsztejn, S. Raabe, C. Strüber, J. Ludwig, S. Yarlagadda, S. Eisebitt, M. J. J. Vrakking, T. Elsaesser, E. T. J. Nibbering, and A. Rouzée, *J. Phys. Chem. Lett.* **10**, 52 (2019).  
<sup>17</sup>M. van Mörbek-Bock, T. Feng, A. Heilmann, L. Ehrentraut, H. Stiel, M. Hennecke, T. Sidiropoulos, C. v. K. Schmising, S. Eisebitt, and M. Schnürer, *Proc. SPIE* **11777**, 117770C (2021).  
<sup>18</sup>J. Probst, C. Braig, and A. Erko, *Appl. Sci.* **10**, 7210 (2020).  
<sup>19</sup>D. J. Nagel, P. G. Burkhalter, C. M. Dozier, J. F. Holzrichter, B. M. Klein, J. M. McMahon, J. A. Stamper, and R. R. Whitlock, *Phys. Rev. Lett.* **33**, 743 (1974).  
<sup>20</sup>M. H. Tuilier and B. Lacour, *J. Phys. B: Atom. Mol. Phys.* **10**, 1407 (1977).  
<sup>21</sup>R. C. Spitzer, R. L. Kauffman, T. Orzechowski, D. W. Phillion, and C. Cerjan, *J. Vac. Sci. Technol. B* **11**, 2986 (1993).  
<sup>22</sup>D. Giulietti and L. A. Gizzi, *Riv. Nuovo Cimento* **21**, 1 (1998).  
<sup>23</sup>U. Vogt, T. Wilhein, H. Stiel, and H. Legall, *Rev. Sci. Instrum.* **75**, 4606 (2004).  
<sup>24</sup>I. Mantouvalou, R. Jung, J. Tümmeler, H. Legall, T. Bidu, H. Stiel, W. Malzer, B. Kanngießer, and W. Sandner, *Rev. Sci. Instrum.* **82**, 066103 (2011).  
<sup>25</sup>I. Mantouvalou, K. Witte, D. Gröttsch, M. Neitzel, S. Günther, J. Baumann, R. Jung, H. Stiel, B. Kanngießer, and W. Sandner, *Rev. Sci. Instrum.* **86**, 035116 (2015).  
<sup>26</sup>P. Wachulak, M. Duda, A. Bartnik, A. Sarzyński, Ł. Węgrzyński, M. Nowak, A. Jancarek, and H. Fiedorowicz, *Opt. Express* **26**, 8260 (2018).  
<sup>27</sup>A. Jonas, K. Dammer, H. Stiel, B. Kanngiesser, R. Sánchez-de-Armas, and I. Mantouvalou, *Anal. Chem.* **92**, 15611 (2020).  
<sup>28</sup>D. Schick, M. Borchert, J. Braenzel, H. Stiel, J. Tümmeler, D. E. Bürgler, A. Firsov, C. von Korff Schmising, B. Pfau, S. Eisebitt, and S. Eisebitt, *Optica* **8**, 1237 (2021).  
<sup>29</sup>J. Tümmeler, R. Jung, H. Stiel, P. V. Nickles, and W. Sandner, *Opt. Lett.* **34**, 1378 (2009).  
<sup>30</sup>D. Strickland and G. Mourou, *Opt. Commun.* **55**, 447 (1985).

- <sup>31</sup>H. Legall, H. Stiel, U. Vogt, H. Schönagel, P.-V. Nickles, J. Tümmeler, F. Scholz, and F. Scholze, *Rev. Sci. Instrum.* **75**, 4981 (2004).
- <sup>32</sup>A. Bergamaschi, M. Andr , R. Barten, C. Borca, M. Br ckner, S. Chiriotti, R. Dinapoli, E. Fr jdh, D. Greiffenberg, T. Huthwelker, A. Kleibert, M. Langer, M. Lebugle, C. Lopez-Cuenca, D. Mezza, A. Mozzanica, J. Raabe, S. Redford, C. Ruder, V. Scagnoli, B. Schmitt, X. Shi, U. Staub, D. Thattil, G. Tinti, C. F. Vaz, S. Vetter, J. Vila-Comamala, and J. Zhang, *Synchrotron Radiat. News* **31**, 11 (2018).
- <sup>33</sup>PiLC, see <https://confluence.desy.de/display/PiLC> for PiLC - DESY confluence, 2022.
- <sup>34</sup>TANGO, see <https://www.tango-controls.org/> for TANGO controls, 2022.
- <sup>35</sup>SARDANA, see <https://www.sardana-controls.org/> for Sardana 3.2.1 documentation, 2022.
- <sup>36</sup>The acquisition is done while the according motors are moving in order to avoid time-consuming starting and stopping of the axis involved in the motion.
- <sup>37</sup>See <https://certif.com/> for CSS - certified scientific software, 2023.
- <sup>38</sup>M. K nnecke, F. A. Akeroyd, H. J. Bernstein, A. S. Brewster, S. I. Campbell, B. Clausen, S. Cottrell, J. U. Hoffmann, P. R. Jemian, D. M nnicke, R. Osborn, P. F. Peterson, T. Richter, J. Suzuki, B. Watts, E. Wintersberger, and J. Wuttke, *J. Appl. Crystallogr.* **48**, 301 (2015).
- <sup>39</sup>M. Brzhezinskaya, A. Firsov, K. Hollmack, T. Kachel, R. Mitzner, N. Pontius, C. Stamm, J.-S. Schmidt, A. F hlisch, and A. Erko, *Proc. SPIE* **8777**, 87771J (2013).
- <sup>40</sup>Z. Yin, J. Rehanek, H. L chel, C. Braig, J. Buck, A. Firsov, J. Viehhaus, A. Erko, and S. Techert, *Opt. Express* **25**, 10984 (2017).
- <sup>41</sup>M. Borchert, D. Engel, C. von Korff Schmising, B. Pfau, S. Eisebitt, and D. Schick, *Optica* **10**(4), 450 (2023).
- <sup>42</sup>A. Jonas, T. Meurer, B. Kanngie er, and I. Mantouvalou, *Rev. Sci. Instrum.* **89**, 026108 (2018).
- <sup>43</sup>S. B. Wilkins, P. D. Hatton, M. D. Roper, D. Prabhakaran, and A. T. Boothroyd, *Phys. Rev. Lett.* **90**, 187201 (2003).
- <sup>44</sup>A. Fert and I. A. Campbell, *J. Phys. F: Met. Phys.* **6**, 849 (1976).
- <sup>45</sup>P. Gr nberg, R. Schreiber, Y. Pang, M. B. Brodsky, and H. Sowers, *Phys. Rev. Lett.* **57**, 2442 (1986).
- <sup>46</sup>M. Elzo, E. Jal, O. Bunau, S. Grenier, Y. Joly, A. Y. Ramos, H. C. N. Tolentino, J. M. Tonnerre, and N. Jaouen, *J. Magn. Magn. Mater.* **324**, 105 (2012).
- <sup>47</sup>D. Schick, *Comput. Phys. Commun.* **266**, 108031 (2021).
- <sup>48</sup>G. van der Laan, B. T. Thole, G. A. Sawatzky, J. B. Goedkoop, J. C. Fuggle, J.-M. Esteva, R. Karnatak, J. P. Remeika, and H. A. Dabkowska, *Phys. Rev. B* **34**, 6529 (1986).
- <sup>49</sup>G. Sch tz, W. Wagner, W. Wilhelm, P. Kienle, R. Zeller, R. Frahm, and G. Materlik, *Phys. Rev. Lett.* **58**, 737 (1987).
- <sup>50</sup>J. St hr, *J. Magn. Magn. Mater.* **200**, 470 (1999).
- <sup>51</sup>J. B. Kortright, D. D. Awschalom, J. St hr, S. D. Bader, Y. U. Idzerda, S. S. P. Parkin, I. K. Schuller, and H.-C. Siegmann, *J. Magn. Magn. Mater.* **207**, 7 (1999).
- <sup>52</sup>B. T. Thole, P. Carra, F. Sette, and G. van der Laan, *Phys. Rev. Lett.* **68**, 1943 (1992).
- <sup>53</sup>P. Carra, B. T. Thole, M. Altarelli, and X. Wang, *Phys. Rev. Lett.* **70**, 694 (1993).
- <sup>54</sup>J. St hr and H. K nig, *Phys. Rev. Lett.* **75**, 3748 (1995).
- <sup>55</sup>J. B. Kortright, S.-K. Kim, T. Warwick, and N. V. Smith, *Appl. Phys. Lett.* **71**, 1446 (1997).
- <sup>56</sup>B. Pfau, C. M. G nther, R. K nnecke, E. Guehrs, O. Hellwig, W. F. Schlotter, and S. Eisebitt, *Opt. Express* **18**, 13608 (2010).
- <sup>57</sup>C. T. Chen, Y. U. Idzerda, H.-J. Lin, N. V. Smith, G. Meigs, E. Chaban, G. H. Ho, E. Pellegrin, and F. Sette, *Phys. Rev. Lett.* **75**, 152 (1995).
- <sup>58</sup>J. F. Peters, J. Miguel, M. A. de Vries, O. M. Toulemonde, J. B. Goedkoop, S. S. Dhesi, and N. B. Brookes, *Phys. Rev. B* **70**, 224417 (2004).
- <sup>59</sup>H. Stiel, J. Braenzel, J. Tuemmler, A. Jonas, I. Mantouvalou, A. Erko, A. Heilmann, M. Moerbeck-Bock, and M. Schnuerer, *Proc. SPIE* **11886**, 1188612 (2021).
- <sup>60</sup>A. Jonas, H. Stiel, L. Gl ggler, D. Dahm, K. Dammer, B. Kanngie er, and I. Mantouvalou, *Opt. Express* **27**, 36524 (2019).
- <sup>61</sup>P. Baumg rtel, M. Witt, J. Baensch, M. Fabarius, A. Erko, F. Sch fers, and H. Schirmacher, *AIP Conf. Proc.* **1741**, 040016 (2016).
- <sup>62</sup>P. Baumg rtel, P. Grundmann, T. Zeschke, A. Erko, J. Viehhaus, F. Sch fers, and H. Schirmacher, *AIP Conf. Proc.* **2054**, 060034 (2019).
- <sup>63</sup>H. Gordon, M. G. Hobby, and N. J. Peacock, *J. Phys. B: Atom. Mol. Phys.* **13**, 1985 (1980).
- <sup>64</sup>NIST, see [https://physics.nist.gov/PhysRefData/ASD/lines\\_form.html](https://physics.nist.gov/PhysRefData/ASD/lines_form.html) for NIST Atomic Spectra Database, 2023.
- <sup>65</sup>J. Kim, K. H. Kim, K. Y. Oang, J. H. Lee, K. Hong, H. Cho, N. Huse, R. W. Schoenlein, T. K. Kim, and H. Ihee, *Chem. Commun.* **52**, 3734 (2016).
- <sup>66</sup>J. Mahl, S. Nepl, F. Roth, M. Borgwardt, C. Saladrigas, B. Toulson, J. Cooper, T. Rahman, H. Bluhm, J. Guo, W. Yang, N. Huse, W. Eberhardt, and O. Gessner, *Faraday Discuss.* **216**, 414 (2019).
- <sup>67</sup>M. Chergui, *Acc. Chem. Res.* **48**, 801 (2015).
- <sup>68</sup>L. Hao, H. Huang, Y. Zhang, and T. Ma, *Adv. Funct. Mater.* **31**, 2100919 (2021).
- <sup>69</sup>S. Liang, X. Wang, Y.-J. Cheng, Y. Xia, and P. M ller-Buschbaum, *Energy Storage Mater.* **45**, 201 (2022).
- <sup>70</sup>K. Witte, C. Streeck, I. Mantouvalou, S. A. Suchkova, H. Lokstein, D. Gr tzsch, W. Martyanov, J. Weser, B. Kanngie er, B. Beckhoff, and H. Stiel, *J. Phys. Chem. B* **120**, 11619 (2016).
- <sup>71</sup>H. Stiel, J. Braenzel, A. Jonas, R. Gnewkow, L. T. Gl ggler, D. Sommer, T. Krist, A. Erko, J. T mmeler, and I. Mantouvalou, *Int. J. Mol. Sci.* **22**, 13463 (2021).
- <sup>72</sup>T. J. Regan III, "X-Ray absorption spectroscopy and microscopy study of ferro - and antiferromagnetic thin films, with applications to exchange anisotropy," Doctoral thesis, Stanford University, 2001.
- <sup>73</sup>J. Pfl ger, J. Fink, G. Crecelius, K. P. Bohnen, and H. Winter, *Solid State Commun.* **44**, 489 (1982).
- <sup>74</sup>M. Tsujimoto, H. Kurata, T. Nemoto, S. Isoda, S. Terada, and K. Kaji, *J. Electron Spectrosc. Relat. Phenom.* **143**, 159 (2005).